


## Functional Renormalization Group Study of Superconductivity in Rhombohedral Trilayer Graphene

Wei Qin<sup>1,\*</sup>, Chunli Huang<sup>1,2</sup>, Tobias Wolf,<sup>1</sup> Nemin Wei,<sup>1</sup> Igor Blinov,<sup>1</sup> and Allan H. MacDonald<sup>1,†</sup>

<sup>1</sup>*Department of Physics, University of Texas at Austin, Austin, Texas 78712, USA*

<sup>2</sup>*Theoretical Division, T-4, Los Alamos National Laboratory, Los Alamos, New Mexico 87545, USA*

 (Received 5 April 2022; revised 1 October 2022; accepted 16 March 2023; published 4 April 2023)

We employ a functional renormalization group approach to ascertain the pairing mechanism and symmetry of the superconducting phase observed in rhombohedral trilayer graphene. Superconductivity in this system occurs in a regime of carrier density and displacement field with a weakly distorted annular Fermi sea. We find that repulsive Coulomb interactions can induce electron pairing on the Fermi surface by taking advantage of momentum-space structure associated with the finite width of the Fermi sea annulus. The degeneracy between spin-singlet and spin-triplet pairing is lifted by valley-exchange interactions that strengthen under the RG flow and develop nontrivial momentum-space structure. We find that the leading pairing instability is *d*-wave-like and spin singlet, and that the theoretical phase diagram versus carrier density and displacement field agrees qualitatively with experiment.

DOI: [10.1103/PhysRevLett.130.146001](https://doi.org/10.1103/PhysRevLett.130.146001)

*Introduction.*—Recent experiments have demonstrated that graphene multilayers can exhibit rich strong-correlation physics [1–18], including broken spin–valley flavor symmetries and superconductivity, when the layers are twisted to magic angles that yield extremely flat moiré superlattice bands [19–23]. Twist angle changes during processing make systematic studies more difficult, however, and devices inevitably have some twist-angle disorder [24]. For this reason, the recent observation [25,26] of superconductivity and broken flavor symmetries in untwisted rhombohedral trilayer graphene (RTG) has been a pleasant surprise. In the regime of displacement field and carrier density where strong correlations have been observed, the normal state is a two-dimensional hole gas with a distorted annular Fermi surface, which has been precisely characterized using quantum oscillation measurements [25,26] that take advantage of the exceptional sample perfection. The strongest superconductivity appears as an instability of a flavor-symmetric paramagnetic normal state and has an in-plane critical magnetic field that seems most compatible with spin-singlet pairing [27,28].

Several ideas have already been explored in connection with superconductivity in RTG [29–35]. Conventional acoustic-phonon-mediated attraction [29] can explain superconductivity only if direct Coulomb interactions between electrons do not play a significant role. The experimental observation of a nearly temperature-independent resistivity up to 20 K suggests that electron-phonon interactions are relatively weak [25], however, arguing against this mechanism. Intervalley coherence fluctuation mediated pairing was proposed as a possibility [30,31,33], motivated by the experimental observation that superconductivity is proximal to a phase transition to a partially

isospin polarized (PIP) phase [30]. However, the observation of a sudden jump in quantum oscillation frequencies between superconducting (SC) and PIP phases [25] indicates that the phase transition is first order and therefore that these critical fluctuations will not be strong. Since superconductivity in RTG is in the clean limit, the Kohn-Luttinger (KL) mechanism [36] has also been considered as a possibility [32,35]. It was demonstrated that superconductivity can arise from the combination of annular Fermi surfaces and long-range Coulomb repulsion in RTG when a random phase approximation (RPA) is employed [32,37].

In this Letter, we apply the functional renormalization group (FRG) method to investigate the pairing mechanism and symmetry in RTG. We start with long-range bare Coulomb interactions, and include a valley-exchange interaction that is  $\sim 100$  times weaker than intra- and intervalley interactions because the Fermi surfaces are small in size compared to the RTG Brillouin zone. We find that the valley-exchange interaction is enhanced under the RG flow and develops nontrivial momentum-space structures that cannot be represented by a simple momentum independent intervalley Hund’s coupling [30,31]. The enhanced valley-exchange interaction breaks valley-SU(2) symmetry and lifts the degeneracy between spin-singlet and spin-triplet pairing. The renormalized pairing interactions develop features at cross-annulus momentum transfers due to inter-Fermi surface particle-hole fluctuations. For experimentally relevant ratios of the annulus radii, these features favor *d*-wave spin-singlet pairing and *p*-wave spin-triplet pairing on the inner and outer Fermi surfaces, respectively. The competition between pairing and particle-hole channel

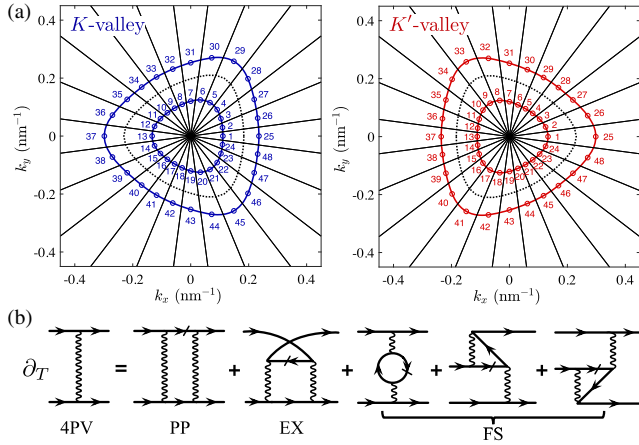


FIG. 1. (a) Patching scheme for the annular Fermi surfaces (solid curves). The momentum space around each valley is divided into 48 patches. The circles on the Fermi surfaces specify the wave vectors at which we evaluate 4PVs. The dotted curves identify the wave vectors at which energy maxima occur along radial directions, and separate patches that belong to the inner and outer Fermi surfaces in our FRG calculations. (b) Diagrammatic representation of the one-loop RG flow equation for 4PVs, including particle-particle (PP), exchange (EX), and forward scattering (FS) contributions. Here the temperature  $T$  is the RG flow time, and the slashes on the propagators denote temperature derivatives [44].

instabilities is sensitive to the Fermi-level density of states as well as the precise annulus shape.

*Model.*—We employ the well established six-band continuum model detailed in the Supplemental Material [38] that accounts for long-range Coulomb interactions, gate and dielectric screening, and all pertinent details of the low-energy electronic structure. In the following calculations, we choose the displacement field-induced electrostatic potential  $\Delta_d = 30$  meV and carrier density  $n_e = -1.75 \times 10^{12}$  cm $^{-2}$  as representative [38]. The corresponding annular Fermi surfaces are illustrated in Fig. 1(a). To capture the competition between superconductivity, intervalley coherence, and spin-polarized half metals in RTG, we employ the temperature-flow FRG scheme because it properly accounts for small- $q$  particle-hole fluctuations [44–46]. The technical details of the present study are similar to earlier works [44,47–49], especially those in multiorbital systems with more than one Fermi surface [50–52]. To implement numerical FRG calculations, we set the initial temperature to  $T_0 \sim 11600$  K [38] and employ the  $N$ -patch scheme [44,53] illustrated in Fig. 1(a).

The one-loop FRG flow equations for four-point vertices (4PVs) with spin-SU(2) symmetry are depicted diagrammatically in Fig. 1(b). These diagrams are similar to KL-mechanism diagrams [36], previously employed to study pairing instabilities in graphene-based systems [32,35,54–61]. The essential difference between the KL diagram and the FRG flow equation is that the former

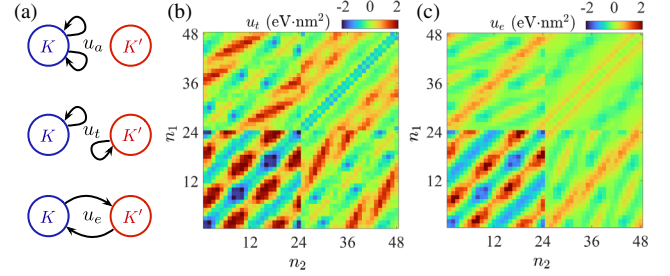


FIG. 2. (a) Schematic diagrams of  $u_{a,t,e}$ . (b)–(c) Renormalized pairing interactions at temperature  $T = 70$  mK, including (b)  $u_t(n_1, \bar{n}_1; \bar{n}_2)$  and (c)  $u_e(n_1, \bar{n}_1; n_2)$ . The bottom-left and top-right  $24 \times 24$  blocks are scatterings on the inner and outer Fermi surfaces, respectively. The remaining blocks are scatterings between the inner and outer Fermi surfaces.

focuses only on the irreducible pairing vertex while the latter retains all 4PVs on an equal footing, making it possible to explore competing orders. Moreover, particle-hole fluctuations that do not develop instabilities can, upon reducing temperature, still give progressively larger contributions to the RG flow of the pairing vertex, leading to an enhancement of the pairing instability. Appealing to standard rescaling and power counting arguments [47,49], we focus on the zero-frequency 4PVs with momenta on the Fermi surfaces. We therefore choose the wave vectors marked by circles in Fig. 1(a) to represent each patch and approximate the 4PVs by  $u(\mathbf{k}_1, \mathbf{k}_2; \mathbf{k}_3) = u(n_1, n_2; n_3)$  for all wave vectors  $\mathbf{k}_i$  in the same patch  $n_i$  [62]. The fourth wave vector is determined by momentum conservation. As shown in Fig. 2(a), the 4PVs can be classified as intravalley ( $u_a$ ), intervalley ( $u_t$ ), or valley exchange ( $u_e$ ) using the definitions

$$\begin{aligned} u_a(n_1, n_2; n_3) &= u(Kn_1, Kn_2; Kn_3), \\ u_t(n_1, n_2; n_3) &= u(Kn_1, K'n_2; K'n_3), \\ u_e(n_1, n_2; n_3) &= u(Kn_1, K'n_2; Kn_3), \end{aligned} \quad (1)$$

where the patch indices are associated with valleys. For example,  $n_2$  in  $u_a$  and  $u_t$  are on  $K$ - and  $K'$ -valley Fermi surfaces, respectively. Time-reversal symmetry requires  $u(\tau_1 n_1, \tau_2 n_2; \tau_3 n_3) = u^*(\bar{\tau}_1 \bar{n}_1, \bar{\tau}_2 \bar{n}_2; \bar{\tau}_3 \bar{n}_3)$ , where  $\bar{n}$  denotes the opposite patch number of  $n$  on the same Fermi surface. Using these conventions, the valley index can be removed from the FRG flow equations (see Supplemental Material [38]).

*Renormalized pairing interaction.*—The initial values of the 4PVs are obtained by patch averaging bare Coulomb interactions using band eigenstates to calculate wave function overlap factors (see Sec. IV in the Supplemental Material [38]). For opposite-valley electron pairing, the relevant 4PVs are  $u_t(n_1, \bar{n}_1; \bar{n}_2)$  and  $u_e(n_1, \bar{n}_1; n_2)$ , where the outgoing momenta belong to  $K$  and  $K'$  valleys. The initial values of  $u_e$  are much weaker (less than 1%) than

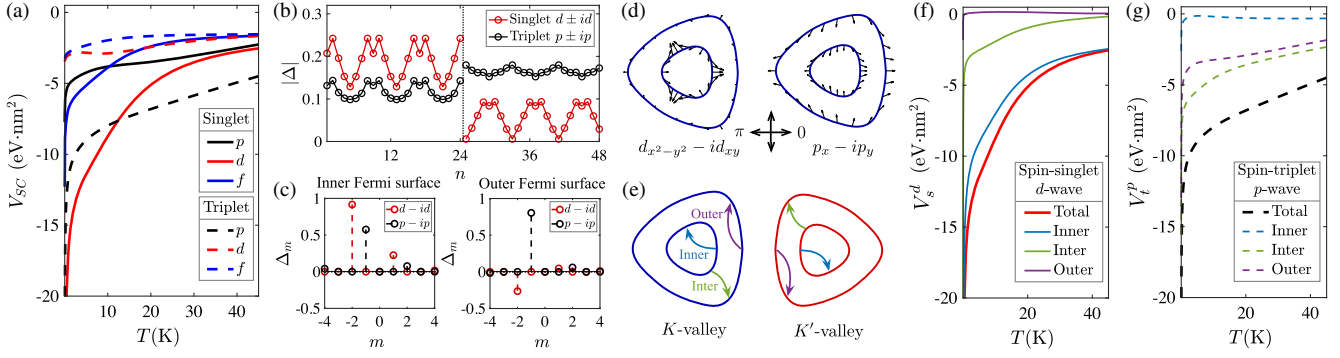


FIG. 3. (a) Temperature flows of pairing interaction in channels distinguished by gap function symmetries. (b) Magnitudes of spin-singlet  $d \pm id$  and spin-triplet  $p \pm ip$  gap functions on the Fermi surfaces. (c) Angular momentum amplitudes  $\Delta_m$  of the gap function on the inner (left) and outer (right) Fermi surfaces. (b)–(c) are calculated at  $T = 70$  mK. (d) Spin-singlet  $d - id$  and spin-triplet  $p - ip$  gap functions on the  $K$ -valley Fermi surfaces, where the length and direction of arrows specify gap amplitude and phase. (e) Schematic diagram of the inner-, inter-, and outer-Fermi surface scatterings that constitute the total pairing interaction  $u_t(n_1, \bar{n}_1; \bar{n}_2, n_2)$ . Similar definitions are used for  $u_e(n_1, \bar{n}_1; n_2, \bar{n}_2)$ . (f)–(g) Contributions from the three types of scatterings illustrated in (e) to pairing interactions in (f) spin-singlet  $d$ -wave and (g) spin-triplet  $p$ -wave channels.

those of  $u_t$  because the magnitude of the intervalley momentum transfer is much larger than the typical size of the annular Fermi surfaces in RTG [38]. As shown in Figs. 2(b) and 2(c),  $u_t$  and  $u_e$  flow to comparable magnitudes as temperature is reduced to  $T = 70$  mK. The effective pairing interactions are

$$V_{s,t} = u_t(n_1, \bar{n}_1; \bar{n}_2, n_2) \pm u_e(n_1, \bar{n}_1; n_2, \bar{n}_2), \quad (2)$$

where the upper (lower) sign is for spin-singlet (spin-triplet) pairing, and the fourth patch index is restored based on momentum conservation. The results shown in Figs. 2(b) and 2(c) indicate that the inner Fermi surface prefers spin-singlet pairing because  $u_t$  and  $u_e$  share similar momentum-space structure, resulting in  $|V_s| > |V_t|$ . In contrast, scatterings across the annular Fermi surfaces and on the outer Fermi surface prefer spin-triplet pairing because  $u_t$  and  $u_e$  possess opposite momentum-space structures, leading to  $|V_s| < |V_t|$ .

**Pairing symmetry.**—The gap function at  $T_c$  is specified by the solution of the linearized gap equation. For the present study, we find that the spin-singlet and spin-triplet gap functions are mainly determined by the momentum-space structures of  $V_{s,t}$  and can be well approximated by the eigenvectors of the largest magnitude negative eigenvalues of  $V_{s,t}$  (see details in the Supplemental Material [38]). Figure 3(a) plots several of the lowest eigenvalues of  $V_{s,t}$  as a function of  $T$ . We find that the strongest spin-singlet and spin-triplet channels are, respectively,  $d$ -wave-like and  $p$ -wave-like, and that both channels have doubly degenerate eigenvectors. Figure 3(b) plots the magnitudes of the chiral  $d \pm id$  and  $p \pm ip$  combinations of these eigenvectors, which are stabilized below the critical temperatures [38]. Note that the leading pairing instability is spin-singlet  $d$ -wave-like because it possesses the lowest

eigenvalue as shown in Fig. 3(a). The deep minima in the gap function on the outer Fermi surface in Fig. 3(b) are due to strong mixing between different angular momentum channels. The terminology used to distinguish  $p$ - and  $d$ -wave pairings is justified by the Fourier coefficients of both gap functions given in Fig. 3(c), where one angular momentum is always dominant. Figure 3(d) illustrates the  $d - id$  and  $p - ip$  gap structures, which are largest on the inner Fermi surface for spin-singlet  $d$ -wave pairing and are comparable in magnitude on the inner and outer Fermi surfaces for spin-triplet  $p$ -wave pairing.

Figures 3(f)–3(g) decompose the spin-singlet  $d$ -wave ( $V_s^d$ ) and spin-triplet  $p$ -wave ( $V_t^p$ ) pairing interactions into contributions from inner-, inter-, and outer-Fermi surface scatterings illustrated in Fig. 3(e) (details in Supplemental Material [38]). We find that  $V_s^d$  is dominated by scattering on the inner Fermi surface while the strongest contribution to  $V_t^p$  is the inter-Fermi surface scattering, which explains the comparable pairing amplitudes on the annular Fermi surfaces in the spin-triplet  $p$ -wave channel. The ultimate pairing symmetry depends on the competition between all three types of scattering, which depends in turn on the Fermi surface shape as we show later.

**Pairing mechanism.**—Figures 4(a) and 4(b) depict the EX diagram contributions to  $u_t$  and  $u_e$ , and the associated intervalley ( $\Pi_{KK'}^{ph}$ ) and intravalley ( $\Pi_{KK}^{ph}$ ) particle-hole susceptibilities are plotted in Figs. 4(c) and 4(d). By comparing Figs. 4(c)–4(d) with Figs. 2(b)–2(c), we find that the momentum-space structures of these susceptibilities are responsible for the momentum-space structures developed in the pairing interactions under FRG, which in turn control the pairing symmetry discussed earlier. For RTG, the momentum-space structures of  $\Pi_{KK'}^{ph}$  and  $\Pi_{KK}^{ph}$  arise primarily from inter-Fermi surface nesting, as illustrated in Figs. 4(d) and 4(e). In fact, the high-temperature

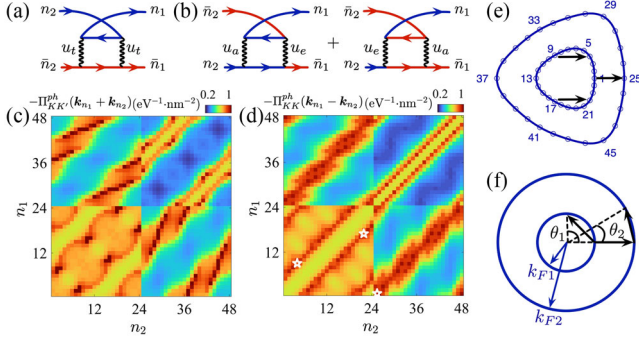


FIG. 4. (a)–(b) EX diagram contributions to  $u_t(n_1, \bar{n}_1; \bar{n}_2, n_2)$  and  $u_e(n_1, \bar{n}_1; n_2, \bar{n}_2)$ , where blue (red) solid lines denote  $K$  ( $K'$ )-valley propagators. (c)–(d) Particle-hole susceptibilities associated with (a)–(b), calculated at  $T = 70$  mK. (e) Three equivalent inter-Fermi-surface nesting wave vectors  $\mathbf{k}_{25} - \mathbf{k}_1 \approx \mathbf{k}_4 - \mathbf{k}_9 \approx \mathbf{k}_{22} - \mathbf{k}_{17}$ , at which  $\Pi_{KK}^{ph}$  peaked:  $(n_1, n_2) = (1, 25)$ ,  $(9, 4)$ , and  $(17, 22)$  marked by stars in (d). (f) Circular annular Fermi surfaces:  $k_{F1,2}$  are the two Fermi wave vectors.  $\theta_{1,2}$  are the angles spanned by  $k_{F2} - k_{F1}$  on the inner and outer Fermi surfaces.

initial stage of the RG flow is dominated by FS processes that screen the long-range Coulomb interaction. The EX enhancement becomes important in the intermediate temperature regime, giving rise to the momentum-space structures of the pairing interactions, which are then amplified by the PP diagram upon further reducing temperature [38]. Therefore, we argue that the KL-like finite angular momentum pairing we have found stems from particle-hole fluctuations that are enhanced by inter-Fermi surface nesting.

It is instructive to analyze the pairing symmetry using the simplified circular Fermi surface model shown in Fig. 4(f) for which the electron energy spectrum is valley independent [38]. Therefore,  $\Pi_{KK}^{ph}(\mathbf{k}_{n_1} - \mathbf{k}_{n_2}) = \Pi_{KK}^{ph}(\theta)$  and  $\Pi_{KK'}^{ph}(\mathbf{k}_{n_1} + \mathbf{k}_{n_2}) = \Pi_{KK}^{ph}(\pi + \theta)$ , where  $\theta$  denotes the angle spanned by  $\mathbf{k}_{n_1} - \mathbf{k}_{n_2}$  on the Fermi surfaces. The  $\pi$ -phase difference between  $\Pi_{KK}^{ph}$  and  $\Pi_{KK'}^{ph}$  is distorted by trigonal warping in Figs. 4(c) and 4(d). Performing Fourier series expansion in  $\theta$ ,

$$-\Pi_{KK}^{ph}(\theta) = \sum_m A_m \cos(m\theta). \quad (3)$$

Since the momentum-space structures of the pairing interactions are primarily determined by those of the particle-hole susceptibilities, we approximate  $\delta u_t(\theta) \propto -\langle u_t \rangle^2 \Pi_{KK'}^{ph}(\theta)$  and  $\delta u_e(\theta) \propto -\langle u_a \rangle \langle u_e \rangle \Pi_{KK}^{ph}(\theta)$ , where  $\langle u_{a,t,e} \rangle$  denote their averaged values over  $\theta$  [38]. Combining with Eqs. (2) and (3), the singlet and triplet pairing interactions in the  $m$ -wave channel  $V_{s,t}^m \propto [(-1)^m \pm 1] A_m$ . As shown in Fig. 4(f), inter-Fermi surface nesting enhances  $-\Pi_{KK}^{ph}(\theta)$  around  $\theta_1$  and  $\theta_2$  on the inner

and outer Fermi surfaces. For this study,  $\theta_1 \sim \pi/2$ , leading to  $-A_2 > |A_1|$ , and hence preferring spin-singlet  $d$ -wave ( $m = 2$ ) pairing on the inner Fermi surface. In contrast,  $\theta_2 < \pi/6$ , which results in  $A_1 > |A_2|$  and prefers spin-triplet  $p$ -wave ( $m = 1$ ) pairing. Inter-Fermi surface scattering always prefers spin-triplet  $p$ -wave pairing because  $-\Pi_{KK}^{ph}(\theta)$  exhibits a maximum at  $\theta = 0$ , as indicated in Fig. 4(d). Overall, the competition between  $d$ -wave singlet and  $p$ -wave triplet pairings in RTG is sensitive to the shape of the annular Fermi surfaces.

*Phase diagram.*—Quantitative prediction of superconducting critical temperature  $T_c$  from FRG calculations stands as a challenging issue [43,47]. Here we provide crude  $T_c$  estimates by solving linearized gap equations with an effective interaction (see details in Sec. VI of Supplemental Material [38]). For the electron pairing channel, the linearized gap equation is

$$\Delta_{s,t}(n) = -\sum_{n_1} \Pi_{KK}^{pp}(n_1) V_{s,t}(n_1, \bar{n}_1; \bar{n}, n) \Delta_{s,t}(n_1), \quad (4)$$

where  $\Delta_{s,t}$  are spin-singlet and spin-triplet order parameters,  $\Pi_{KK}^{pp}(n_1)$  denotes the particle-particle susceptibility, and the renormalized pairing interactions  $V_{s,t}$  are given by Eq. (2). Since both  $\Pi_{KK}^{pp}$  and  $V_{s,t}$  are temperature dependent,  $T_c$  is estimated for each channel as the temperature at which the corresponding eigenvalue of  $-\Pi_{KK}^{pp} V_{s,t}$  equals 1.

We have also explored the competition between pairing and particle-hole channel instabilities. Table I summarizes several typical particle-hole channel instabilities (see details in Sec. VI of Supplemental Material [38]). As shown in Fig. 5(a), for large hole densities that are associated with relatively thick annular Fermi seas, spin-singlet  $d$ -wave pairing is the leading instability. The corresponding  $T_c$  exhibits a domelike behavior vs hole density that is qualitatively consistent with experimental observations [25]. We note that experimental signatures of a SC state do appear to be present in the longitudinal resistivity at hole densities that exceed the region that can currently be identified as in the SC dome [25]. The data

TABLE I. Matrix structures and symmetries under time-reversal  $T$  and inversion  $C_2$  operations of the order parameters for Pomeranchuk instability (PI), valley polarization (VP), ferromagnetism or antiferromagnetism (FM/AFM), and intervalley charge and spin coherence (IVC/IVS). Here FM and AFM are distinguished by identical and opposite spin polarizations in two valleys,  $s_{x,y,z}$  and  $\tau_{x,y,z}$  are Pauli matrices in spin and valley subspaces, and  $\mathcal{K}$  denotes the complex conjugate.

Particle-hole instability	PI	VP	FM	AFM	IVC	IVS
Order parameter	$s_0 \tau_0$	$s_0 \tau_z$	$s_z \tau_0$	$s_z \tau_z$	$s_0 \tau_{x,y}$	$s_z \tau_{x,y}$
$T = i s_y \tau_x \mathcal{K}$	✓	✗	✗	✓	✓	✗
$C_2 = s_0 \tau_x$	✓	✗	✓	✗	✗	✗

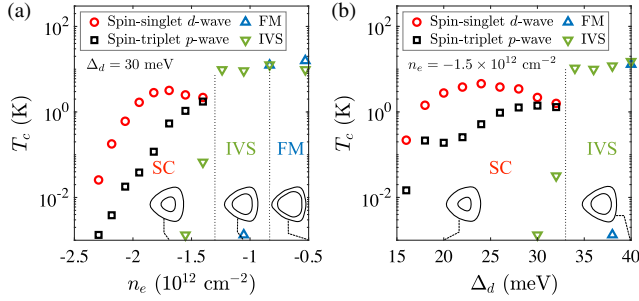


FIG. 5. Phase diagrams as function of (a)  $n_e$  and (b)  $\Delta_d$ . The inserts depict the annular Fermi surfaces for several typical values of  $n_e$  and  $\Delta_d$  that are associated with the SC, IVS and FM states. These results are obtained by choosing dielectric constant  $\epsilon = 4$  and gate-sample distance  $d_s = 40$  nm.

seem to be consistent with the notion that superconductivity survives to higher hole densities, as in our calculations, albeit with substantially decreased  $T_c$ . By decreasing the hole density and moving the Fermi level toward the VHS [see Fig. 5(a)], the PIP state seen in experiment appears consistent with an IVS state emerging first and then being replaced by the FM state. In our calculations, these two states compete closely when the Fermi level of the system approaches the VHS. Since the averaged value of  $u_e$  is positive, IVS and FM always dominate over IVC and AFM (see Supplemental Material [38]). Similar behavior is revealed in the phase diagram vs  $\Delta_d$  for a given  $n_e$  in Fig. 5(b). The qualitative features of these phase diagrams are therefore in good agreement with experimental observations [25].

*Discussion.*—Numerical estimates of superconducting  $T_c$ 's depend on model parameters, such as the dielectric constant  $\epsilon$  (see Supplemental Material [38]). One general trend is that stronger Coulomb interaction results in higher  $T_c$ , contradictory to the acoustic-phonon-mediated superconductivity [29]. The experimental phase diagram [25] shows that the PIP (IVS) state emerges at a larger hole density than in our theoretical estimation. If the stability region of the IVS state is expanded to agree with experiment, it intervenes before the peak of the superconducting dome is reached. This shift would avoid the region in the phase diagram where the  $p$ -wave spin-triplet pairing state becomes nearly degenerate with or even dominates over the  $d$ -wave spin-singlet pairing [38]. In fact, an accurate determination of the phase boundary is obviously very demanding and beyond the scope of the present FRG study. The sudden jumps of the  $T_c$ 's for the IVS and FM states shown in Fig. 5 arise from the fact that the particle-hole susceptibilities possess maxima at finite temperatures due to proximity to the VHS [38]. Such a jump in  $T_c$  for the IVS state is consistent with experimental observation of the jump in quantum oscillation frequency between SC and PIP phases [25]. We have explored the effects of changing other model parameters [38]. The resulting phase diagrams share similar qualitative features with Fig. 5.

The present study explains the spin-singlet SC dome observed in RTG in terms of inter-Fermi-surface nesting that leads to  $d$ -wave singlet pairing. We find that the Fermi surface geometry plays the key role in determining pairing symmetry and predict that the strongest  $d$ -wave spin-singlet pairing emerges when the ratio of the enclosed areas of the inner and outer Fermi surfaces is  $r = S_{\text{in}}/S_{\text{out}} \approx 0.176$ , close to the value of 0.2 measured near the SC dome [25,38]. Larger values of  $r$  obtained by increasing  $\Delta_d$  or  $n_e$  lead to first-order spin or valley ferromagnetic phase transitions that reconstruct the Fermi surface [63], removing the annulus and preempting the pairing instability.

The authors are grateful for helpful interactions with Andrea F. Young, Haoxin Zhou, and Jihang Zhu. This work was supported by the U.S. Department of Energy, Office of Science, Basic Energy Sciences, under Award No. DE-SC0022106. The work done at LANL was carried out under the auspices of the U.S. DOE NNSA under Contract No. 89233218CNA000001 through the LDRD Program. T. M. R. W. is grateful for the financial support from the Swiss National Science Foundation (Postdoc.Mobility Grant No. 203152). Numerical calculations were performed using supercomputing resources at the Texas Advanced Computing Center (TACC).

\* weiqin@utexas.edu

† macd@physics.utexas.edu

- [1] Y. Cao, V. Fatemi, S. Fang, K. Watanabe, T. Taniguchi, E. Kaxiras, and P. Jarillo-Herrero, Unconventional superconductivity in magic-angle graphene superlattices, *Nature (London)* **556**, 43 (2018).
- [2] Y. Cao, V. Fatemi, A. Demir, S. Fang, S. L. Tomarken, J. Y. Luo, J. D. Sanchez-Yamagishi, K. Watanabe, T. Taniguchi, E. Kaxiras, R. C. Ashoori, and P. Jarillo-Herrero, Correlated insulator behaviour at half-filling in magic-angle graphene superlattices, *Nature (London)* **556**, 80 (2018).
- [3] M. Yankowitz, S. Chen, H. Polshyn, Y. Zhang, K. Watanabe, T. Taniguchi, D. Graf, A. F. Young, and C. R. Dean, Tuning superconductivity in twisted bilayer graphene, *Science* **363**, 1059 (2019).
- [4] X. Lu, P. Stepanov, W. Yang, M. Xie, M. A. Aamir, I. Das, C. Urgell, K. Watanabe, T. Taniguchi, G. Zhang, A. Bachtold, A. H. MacDonald, and D. K. Efetov, Superconductors, orbital magnets and correlated states in magic-angle bilayer graphene, *Nature (London)* **574**, 653 (2019).
- [5] L. Balents, C. R. Dean, D. K. Efetov, and A. F. Young, Superconductivity and strong correlations in moiré flat bands, *Nat. Phys.* **16**, 725 (2020).
- [6] P. Stepanov, I. Das, X. Lu, A. Fahimniya, K. Watanabe, T. Taniguchi, F. H. L. Koppens, J. Lischner, L. Levitov, and D. K. Efetov, Untying the insulating and superconducting orders in magic-angle graphene, *Nature (London)* **583**, 375 (2020).
- [7] Y. Saito, J. Ge, K. Watanabe, T. Taniguchi, and A. F. Young, Independent superconductors and correlated insulators in twisted bilayer graphene, *Nat. Phys.* **16**, 926 (2020).

- [8] D. Wong, K. P. Nuckolls, M. Oh, B. Lian, Y. Xie, S. Jeon, K. Watanabe, T. Taniguchi, B. A. Bernevig, and A. Yazdani, Cascade of electronic transitions in magic-angle twisted bilayer graphene, *Nature (London)* **582**, 198 (2020).
- [9] U. Zondiner, A. Rozen, D. Rodan-Legrain, Y. Cao, R. Queiroz, T. Taniguchi, K. Watanabe, Y. Oreg, F. von Oppen, A. Stern, E. Berg, P. Jarillo-Herrero, and S. Ilani, Cascade of phase transitions and Dirac revivals in magic-angle graphene, *Nature (London)* **582**, 203 (2020).
- [10] X. Liu, Z. Wang, K. Watanabe, T. Taniguchi, O. Vafek, and J. I. A. Li, Tuning electron correlation in magic-angle twisted bilayer graphene using Coulomb screening, *Science* **371**, 1261 (2021).
- [11] J. M. Park, Y. Cao, K. Watanabe, T. Taniguchi, and P. Jarillo-Herrero, Tunable strongly coupled superconductivity in magic-angle twisted trilayer graphene, *Nature (London)* **590**, 249 (2021).
- [12] Z. Hao, A. M. Zimmerman, P. Ledwith, E. Khalaf, D. H. Najafabadi, K. Watanabe, T. Taniguchi, A. Vishwanath, and P. Kim, Electric field-tunable superconductivity in alternating-twist magic-angle trilayer graphene, *Science* **371**, 1133 (2021).
- [13] P. Stepanov, M. Xie, T. Taniguchi, K. Watanabe, X. Lu, A. H. MacDonald, B. A. Bernevig, and D. K. Efetov, Competing Zero-Field Chern Insulators in Superconducting Twisted Bilayer Graphene, *Phys. Rev. Lett.* **127**, 197701 (2021).
- [14] Y. Saito, F. Yang, J. Ge, X. Liu, T. Taniguchi, K. Watanabe, J. I. A. Li, E. Berg, and A. F. Young, Isospin pomeranchuk effect in twisted bilayer graphene, *Nature (London)* **592**, 220 (2021).
- [15] Y. Cao, J. M. Park, K. Watanabe, T. Taniguchi, and P. Jarillo-Herrero, Pauli-limit violation and re-entrant superconductivity in moiré graphene, *Nature (London)* **595**, 526 (2021).
- [16] Y. Choi, H. Kim, Y. Peng, A. Thomson, C. Lewandowski, R. Polski, Y. Zhang, H. S. Arora, K. Watanabe, T. Taniguchi, J. Alicea, and S. Nadj-Perge, Correlation driven topological phases in magic-angle twisted bilayer graphene, *Nature (London)* **589**, 536 (2021).
- [17] Y. Choi, H. Kim, C. Lewandowski, Y. Peng, A. Thomson, R. Polski, Y. Zhang, K. Watanabe, T. Taniguchi, J. Alicea, and S. Nadj-Perge, Interaction-driven band flattening and correlated phases in twisted bilayer graphene, *Nat. Phys.* **17**, 1375 (2021).
- [18] A. Jaoui, I. Das, G. D. Battista, J. Díez-Mérida, X. Lu, K. Watanabe, T. Taniguchi, H. Ishizuka, L. Levitov, and D. K. Efetov, Quantum critical behaviour in magic-angle twisted bilayer graphene, *Nat. Phys.* **18**, 633 (2022).
- [19] R. Bistritzer and A. H. MacDonald, Moiré bands in twisted double-layer graphene, *Proc. Natl. Acad. Sci. U.S.A.* **108**, 12233 (2011).
- [20] E. Khalaf, A. J. Kruchkov, G. Tarnopolsky, and A. Vishwanath, Magic angle hierarchy in twisted graphene multilayers, *Phys. Rev. B* **100**, 085109 (2019).
- [21] C. Mora, N. Regnault, and B. A. Bernevig, Flatbands and Perfect Metal in Trilayer Moiré Graphene, *Phys. Rev. Lett.* **123**, 026402 (2019).
- [22] Z. Zhu, S. Carr, D. Massatt, M. Luskin, and E. Kaxiras, Twisted Trilayer Graphene: A Precisely Tunable Platform for Correlated Electrons, *Phys. Rev. Lett.* **125**, 116404 (2020).
- [23] C. Lei, L. Linhart, W. Qin, F. Libisch, and A. H. MacDonald, Mirror symmetry breaking and lateral stacking shifts in twisted trilayer graphene, *Phys. Rev. B* **104**, 035139 (2021).
- [24] A. Uri, S. Grover, Y. Cao, J. A. Crosse, K. Bagani, D. Rodan-Legrain, Y. Myasoedov, K. Watanabe, T. Taniguchi, P. Moon, M. Koshino, P. Jarillo-Herrero, and E. Zeldov, Mapping the twist-angle disorder and Landau levels in magic-angle graphene, *Nature (London)* **581**, 47 (2020).
- [25] H. Zhou, T. Xie, T. Taniguchi, K. Watanabe, and A. F. Young, Superconductivity in rhombohedral trilayer graphene, *Nature (London)* **598**, 434 (2021).
- [26] H. Zhou, T. Xie, A. Ghazaryan, T. Holder, J. R. Ehrets, E. M. Spanton, T. Taniguchi, K. Watanabe, E. Berg, M. Serbyn, and A. F. Young, Half- and quarter-metals in rhombohedral trilayer graphene, *Nature (London)* **598**, 429 (2021).
- [27] B. S. Chandrasekhar, A note on the maximum critical field of high-field superconductor, *Appl. Phys. Lett.* **1**, 7 (1962).
- [28] A. M. Clogston, Upper Limit for the Critical Field in Hard Superconductors, *Phys. Rev. Lett.* **9**, 266 (1962).
- [29] Y.-Z. Chou, F. Wu, J. D. Sau, and S. Das Sarma, Acoustic-Phonon-Mediated Superconductivity in Rhombohedral Trilayer Graphene, *Phys. Rev. Lett.* **127**, 187001 (2021).
- [30] S. Chatterjee, T. Wang, E. Berg, and M. P. Zaletel, Inter-valley coherent order and isospin fluctuation mediated superconductivity in rhombohedral trilayer graphene, *Nat. Commun.* **13**, 6013 (2022).
- [31] Y.-Z. You and A. Vishwanath, Kohn-Luttinger superconductivity and inter-valley coherence in rhombohedral trilayer graphene, *Phys. Rev. B* **105**, 134524 (2022).
- [32] A. Ghazaryan, T. Holder, M. Serbyn, and E. Berg, Unconventional Superconductivity in Systems with Annular Fermi Surfaces: Application to Rhombohedral Trilayer Graphene, *Phys. Rev. Lett.* **127**, 247001 (2021).
- [33] Z. Dong and L. Levitov, Superconductivity in the vicinity of an isospin-polarized state in a cubic Dirac band, *arXiv*: 2109.01133.
- [34] A. L. Szabó and B. Roy, Metals, fractional metals, and superconductivity in rhombohedral trilayer graphene, *Phys. Rev. B* **105**, L081407 (2022).
- [35] T. Cea, P. A. Pantaleón, V. T. Phong, and F. Guinea, Superconductivity from repulsive interactions in rhombohedral trilayer graphene: A Kohn-luttinger-like mechanism, *Phys. Rev. B* **105**, 075432 (2022).
- [36] W. Kohn and J. M. Luttinger, New Mechanism for Superconductivity, *Phys. Rev. Lett.* **15**, 524 (1965).
- [37] S. Raghu and S. A. Kivelson, Superconductivity from repulsive interactions in the two-dimensional electron gas, *Phys. Rev. B* **83**, 094518 (2011).
- [38] See Supplemental Material at <http://link.aps.org/supplemental/10.1103/PhysRevLett.130.146001> for more details, which includes Refs. [39–43].
- [39] F. Zhang, B. Sahu, H. Min, and A. H. MacDonald, Band structure of ABC-stacked graphene trilayers, *Phys. Rev. B* **82**, 035409 (2010).
- [40] A. Laturia, M. L. Van de Put, and W. G. Vandenberghe, Dielectric properties of hexagonal boron nitride and

- transition metal dichalcogenides: From monolayer to bulk, *2D Mater. Appl.* **2**, 6 (2018).
- [41] F. Wu, A. H. MacDonald, and I. Martin, Theory of Phonon-Mediated Superconductivity in Twisted Bilayer Graphene, *Phys. Rev. Lett.* **121**, 257001 (2018).
- [42] M. Koshino, N. F. Q. Yuan, T. Koretsune, M. Ochi, K. Kuroki, and L. Fu, Unconventional Superconductivity and Density Waves in Twisted Bilayer Graphene, *Phys. Rev. X* **8**, 041041 (2018).
- [43] A. V. Chubukov, D. V. Efremov, and I. Eremin, Magnetism, superconductivity, and pairing symmetry in iron-based superconductors, *Phys. Rev. B* **78**, 134512 (2008).
- [44] C. Honerkamp and M. Salmhofer, Temperature-flow renormalization group and the competition between superconductivity and ferromagnetism, *Phys. Rev. B* **64**, 184516 (2001).
- [45] W. Metzner, C. Castellani, and C. D. Castro, Fermi systems with strong forward scattering, *Adv. Phys.* **47**, 317 (1998).
- [46] C. J. Halboth and W. Metzner, Renormalization-group analysis of the two-dimensional Hubbard model, *Phys. Rev. B* **61**, 7364 (2000).
- [47] R. Shankar, Renormalization-group approach to interacting fermions, *Rev. Mod. Phys.* **66**, 129 (1994).
- [48] C. Honerkamp, M. Salmhofer, N. Furukawa, and T. M. Rice, Breakdown of the Landau-Fermi liquid in two dimensions due to umklapp scattering, *Phys. Rev. B* **63**, 035109 (2001).
- [49] W. Metzner, M. Salmhofer, C. Honerkamp, V. Meden, and K. Schönhammer, Functional renormalization group approach to correlated fermion systems, *Rev. Mod. Phys.* **84**, 299 (2012).
- [50] F. Wang, H. Zhai, Y. Ran, A. Vishwanath, and D.-H. Lee, Functional Renormalization-Group Study of the Pairing Symmetry and Pairing Mechanism of the FeAs-Based High-Temperature Superconductor, *Phys. Rev. Lett.* **102**, 047005 (2009).
- [51] R. Thomale, C. Platt, W. Hanke, and B. A. Bernevig, Mechanism for Explaining Differences in the Order Parameters of FeAs-Based and FeP-Based Pnictide Superconductors, *Phys. Rev. Lett.* **106**, 187003 (2011).
- [52] C. Platt, W. Hanke, and R. Thomale, Functional renormalization group for multi-orbital Fermi surface instabilities, *Adv. Phys.* **62**, 453 (2013).
- [53] D. Di Sante, M. Medvidović, A. Toschi, G. Sangiovanni, C. Franchini, A. M. Sengupta, and A. J. Millis, Deep Learning the Functional Renormalization Group, *Phys. Rev. Lett.* **129**, 136402 (2022).
- [54] J. González, Kohn-Luttinger superconductivity in graphene, *Phys. Rev. B* **78**, 205431 (2008).
- [55] J. González, Magnetic and Kohn-Luttinger instabilities near a Van Hove singularity: Monolayer versus twisted bilayer graphene, *Phys. Rev. B* **88**, 125434 (2013).
- [56] M. Yu. Kagan, V. V. Val'kov, V. A. Mitskan, and M. M. Korovushkin, The Kohn-Luttinger superconductivity in idealized doped graphene, *Solid State Commun.* **188**, 61 (2014).
- [57] M. Y. Kagan, V. V. Val'kov, V. A. Mitskan, and M. M. Korovushkin, The Kohn-Luttinger effect and anomalous pairing in new superconducting systems and graphene, *J. Exp. Theor. Phys.* **118**, 995 (2014).
- [58] M. Y. Kagan, V. A. Mitskan, and M. M. Korovushkin, Phase diagram of the Kohn-Luttinger superconducting state for bilayer graphene, *Eur. Phys. J. B* **88**, 157 (2015).
- [59] Z. A. H. Goodwin, F. Corsetti, A. A. Mostofi, and J. Lischner, Attractive electron-electron interactions from internal screening in magic-angle twisted bilayer graphene, *Phys. Rev. B* **100**, 235424 (2019).
- [60] J. González and T. Stauber, Kohn-Luttinger Superconductivity in Twisted Bilayer Graphene, *Phys. Rev. Lett.* **122**, 026801 (2019).
- [61] V. T. Phong, P. A. Pantaleón, T. Cea, and F. Guinea, Band structure and superconductivity in twisted trilayer graphene, *Phys. Rev. B* **104**, L121116 (2021).
- [62] In our convention  $u(\mathbf{k}_1, \mathbf{k}_2; \mathbf{k}_3)$  represents the Coulomb matrix elements where the incoming momenta  $\mathbf{k}_3 - \mathbf{k}_1 - \mathbf{k}_2$  and  $\mathbf{k}_3$  scatter, respectively, into outgoing momenta  $\mathbf{k}_1$  and  $\mathbf{k}_2$ .
- [63] C. Huang, T. Wolf, W. Qin, N. Wei, I. Blinov, and A. H. MacDonald, Spin and orbital metallic magnetism in rhombohedral trilayer graphene, *Phys. Rev. B* **107**, L121405 (2023).